LAWRENCE
LIVERMORE
NATIONAL
LABORATORY

UCRL-JRNL-201121

# Explosive Chemistry: Simulating the Chemistry of Energetic Materials at Extreme Conditions

M. Riad Manaa, Laurence E. Fried, Evan J. Reed

November 20, 2003

Journal of Computer-Aided Materials Design

## Disclaimer

# Explosive Chemistry: Simulating the Chemistry of Energetic Materials at Extreme Conditions

M. Riad Manaa and Laurence E. Fried

Lawrence Livermore National Laboratory, Energetic Materials Center,

P.O. Box 808, L-282, Livermore, California 94551

and

Evan J. Reed

Department of Physics, Massachusetts Institute of Technology,

Cambridge, MA 02139

**To be submitted to Journal of Computer-Aided Materials Design**

This work was performed under the auspices of the U.S. Department of Energy by the University of California, Lawrence Livermore National Laboratory under contract No. W-7405-Eng-48.

# 1. INTRODUCTION

In the brief instant of a high-explosive detonation, the shock wave produces a pressure 500,000 times that of the Earth's atmosphere, the detonation wave travels as fast as 10 kilometers per second, and internal temperatures soar up to 5,500 Kelvin. As the shock propagates through the energetic material, the rapid heating coupled with compression that results in almost 30% volume reduction, initiate complex chemical reactions. A dense, highly reactive supercritical fluid is established behind the propagating detonation front. Energy release from the exothermic chemical reactions serve in turn to drive and sustain the detonation process until complete reactivity is reached. Several experimental results suggest the existence of strong correlations between the applied mechanical stress and shocks, the local heterogeneity and defects (dislocations, vacancies, cracks, impurities, etc.), and the onset of chemical reactions. [1-6] The reaction chemistry of energetic materials at high pressure and temperature is, therefore, of considerable importance in understanding processes that these materials experience under impact and detonation conditions. Chemical decomposition models are critical ingredients in order to predict, among other things, the measured times to explosion and the conditions for ignition of hot spots, [7] localized regions of highly concentrated energy associated with defects. [8-10] To date, chemical kinetic rates of condense-phase energetic materials at detonation conditions are virtually non-existent, and basic questions such as: (a) which bond in a given energetic molecule breaks first, and (b) what type of chemical reactions (unimolecular versus bimolecular, etc.) that dominate early in the decomposition process, are still largely unknown.

At present, computer simulations at the atomistic level provide the best access to the short time scale processes (~100 femtoseconds to a few tens of picoseconds) occurring in regions of extreme conditions. Computational investigations aspire to unravel at the molecular

level, among others, the initiation mechanism(s), detailed decomposition pathways, and the kinetic rate laws at high-pressure and temperature. The ultimate objective of such studies is to construct accurate and predictive models of performance and sensitivity for the development of new energetic materials. [11]

Molecular dynamics simulations have been successfully applied in the study of chemical events at high-pressure (density) and temperature in recent time. Three levels of approximations for the calculations of interatomic forces now makes it possible to treat systems from a few hundreds to thousands of atoms for a time of up to a 100 picosecond. First principles, density functional/molecular dynamics simulations have been demonstrated recently for water, ammonia, and methane at temperatures up to 7000 K and pressures of up to 300 GPa. [12,13] Semi-empirical methods such as tight-binding has been used to study the chemical events of shocked benzene, [14] shocked methane, [15], and the chemistry of dense HMX explosive at 3500 K. [16] Molecular dynamics simulations using empirical bond order potential have been performed to study the shock – induced chemistry in condensed-phase hydrocarbons of acetylene, ethylene, and methane, [17] and a reactive force field (ReaxFF) has been developed to study the induced chemistry of the nitramine explosive RDX at shock conditions. [18]

In this article, we review our recent work in applying computational techniques to investigate the electronic structure aspects and chemistry of energetic materials at high-pressure and /or high temperature. Several mechanisms have been proposed for the initial events of energetic materials at high-pressure. We study the effect of high-pressure (both uniform and uniaxial) at the electronic energy band-gap and the first chemical event of a prototypical energetic material, that of nitromethane. We explore the validity of a proposed shear-induced local metallization via molecular bond bending in the insensitive explosive

triamino-trinitrobenzene (TATB). We also report on a molecular dynamics (MD) simulation of 1,3,5, 7-tetranitro-1, 3,5,7-tetraazacyclooctane (HMX), a widely used explosive material, at conditions of high density and temperature similar to that encounter under detonation. Finally, we review a new multi-scale computational tool recently developed to model the shock-induced chemistry of energetic materials at the atomistic level, and report its applicability as a case study to solid nitromethane experiencing a shock with a speed of 7 km/s.

## 2. INITIATION MODELS OF ENERGETIC MATERIALS

The initial response of a heterogeneous energetic molecular solid to a sudden compression is of interest in order to understand the various energy transfer processes that occur under shock compression. Several models have been proposed throughout the last few decades. Coffey [10,19,20] postulated that the initiation process is due to tunneling of dislocations in a solid; when the shock velocities are sufficiently high, the dislocations can have energy adequate to directly pump the internal vibrational modes of the constituent molecules. The vibrational energy up-pumping model [9] suggests that the shock wave produce a bath of excited phonons absorbed by the lowest vibrational modes of molecules that make up the crystal. Increased phonon absorption and intramolecular vibrational energy redistribution (IVR) lead to excitation of higher frequency modes, eventually reaching an equilibrium transition state, and proceeding to chemical bond breakage and the subsequent chemical reactions. A simple formula for the total energy transfer rate into a given vibron band in terms of the density of vibrational states and the vibron-phonon coupling was subsequently derived. [21] The phonon upconversion rates, based on small cubic anharmonic terms, were shown to correlate with the sensitivity in such explosives as TATB, HMX and lead styphnate. Tarver [22] discussed multiple roles of highly vibrationally excited molecules in the reaction zones of

detonation waves for his model of the nonequilibrium Zeldovich-von Neumann-Doring theory of self-sustaining detonations. [23-25]

Noting that detonation fronts propagate too fast for the chemical reactions that drive them to be thermally activated, Gilman, on the other hand, proposed that the compression in such fronts causes local metallization in the unreacted material when either the density, or the bending of covalent bonds, reaches a critical level. [26] In covalently bonded materials, when bonds are stretched and bent, there are regions in the nuclear configuration space where the energies of the highest occupied molecular orbital (HOMO) and that of the lowest unoccupied molecular orbital (LUMO) become degenerate. In periodic solids, the HOMO-LUMO gaps develop into band gaps, hence, a band gap closure and the delocalization of the valence band electrons (metallization) would be achieved as molecules are confined to the intersection regions. Since a detonation front causes compression and shears in the unreacted materials, it was noted that for covalently bonded materials, bond-bending is more important than bond-compression because the associated force constants are smaller. [27] HUMO-LUMO energy band closure due to bond-bending allows the electrons in the bonding states to expand at constant volume, and thus the occurrence of fast reactions. Evidence cited in support of critical shear-induced metallization is the correlation of HUMO-LUMO energy gap of a homologous series of amino-nitro-benzenes explosives, studied through their 'shake-up' spectra, with their sensitivity to shocks. [28]

Recently, we investigated the effect of bond-bending on the energy band-gap of the covalent molecular solid TATB (1,3,5-triamino-2,4,6-trinitrobenzene), using first-principal quantum mechanical calculations. [29] The object was to identify the molecular deformation parameters responsible for lowering the HOMO-LUMO gap. Molecular TATB consists of benzene-like rings of carbon atoms that are bonded to alternating amino ($-NH_2$) and nitro

($NO_2$) groups. The crystal structure consists of hydrogen bonded molecular sheets akin to graphite, contributing to its formidable stability as manifested in the high melting point (>300 °C) and the lack of solubility in most common solvents. The choice of TATB serves as an example of a nitro- containing molecule with several degrees of freedom, and for which relevant experimental results exist. Extension to other molecular solids containing the nitro group such as nitromethane is applicable; [30] as well as other modified benzenes.

A series of electronic structure calculations were performed based on density-functional theory. The optimized unit cell of TATB with fully relaxed atomic positions yielded a band gap of 2.5 eV, which is in good agreement with the experimentally determined band gap that is reported to be in the range 2.7 - 3.1 eV. [28] Since the LUMO is a $\pi^*$ orbital localized on the -$NO_2$ group, any reduction in the band gap must involve motions associated with this group. Deformation of this group (in the whole of the unit cell) has been induced in several ways: rotation around the carbon-nitrogen bond, decreasing the O-N-O angle, and out of plane bending with respect to the angle $\gamma$ as in Figure 1 . For each of these cases, the N-O bond was also varied by ±0.5 Å. Neither the rotation around the C-N bond, nor the in-plane bending of the O-N-O angle showed any appreciable decrease in the band gap. The bending through $\gamma$, combined with a stretch in both N-O bonds, exhibited a significant drop and eventually a closure in the band gap. Figure 2 shows the band structure near the Fermi level for this bending motion, clearly indicating that TATB crystals have been induced to become a metal. The molecular geometry of this configuration corresponds to $\gamma = 55°$, while the N-O bond distance has undergone a stretch from 1.274 Å at its relaxed configuration to 1.377 Å. At this configuration, the crystal has acquired an amount of 0.1 eV/atom of energy. This amount of energy is of the same order as for the HOMO-LUMO separation of the insulator structure. Thus, the amount of work required to induce metallization is on the order of the HOMO-LUMO energy gap. The results are in agreement with Gilman's postulation that

metallization would be achieved with little change in bond lengths, but with marked change in bond angles. [27]

The critical shear (bending) angle responsible for the vanishing of the energy band gap in TATB is achieved at near constant volume. This was verified through a constraint optimization of the unit cell: the angle $\gamma$ was constrained to its critical value, while allowing the relaxation of the rest of atomic positions. Results show that the cell volume was reduced by about 5%. It should be stressed, however, that this small deviation is superfluous in origin, because the location of the critical bending angle was performed without optimization in the full molecular configuration space.

The bending motion of the nitro group that causes insulator-metal transition is not expected to come about under static high-pressure, as is demonstrated later for the case of solid nitromethane with pressure up to 200 gigapascals, [31,32] and TATB under unaxial pressure. [33] In addition to shear strain, this motion might be expected to occur under sudden dynamical stresses for which high-speed molecular collisions are ubiquitous, as is the case in shock phenomena.

Other simulations considered band-gap properties of imperfect energetic molecular solids, such as the cyclotrimethylene trinitramine (RDX) And pentaetythritol tetranitrate (PETN) crystals with vacancies and dislocations. [34-38] These studies have indicated that compression of the RDX crystal in the presence of single [35-37] and dimmer [34,38] vacancies reduces the optical gap of this material appreciably, thus decreasing the excitation energy needed for the insulator-metal phase transition. Specifically, these calculations showed that the edge dislocations cause a dramatic reduction of the optical gap due to the splitting of the local electronic states from both the valence and conduction bands. These findings have in turn prompted a mechanism based on electronic excitations induced by the impact wave

propagating through the crystal. [39] According to this hypothesis, the pressure exerted by the impact wave front causes the dramatic reduction of the band gap to nearly zero values and results in the breakage of the N-$NO_2$ chemical bond in RDX, thus initiating detonation and chemical chain reactions.

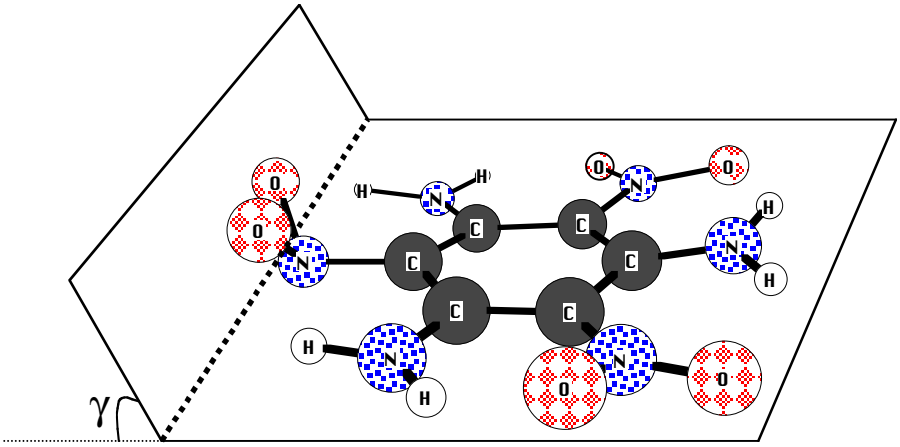


Figure 1. Schematic representation of the bending motion of the $NO_2$ group in molecular TATB. Atoms are designated by corresponding symbols.

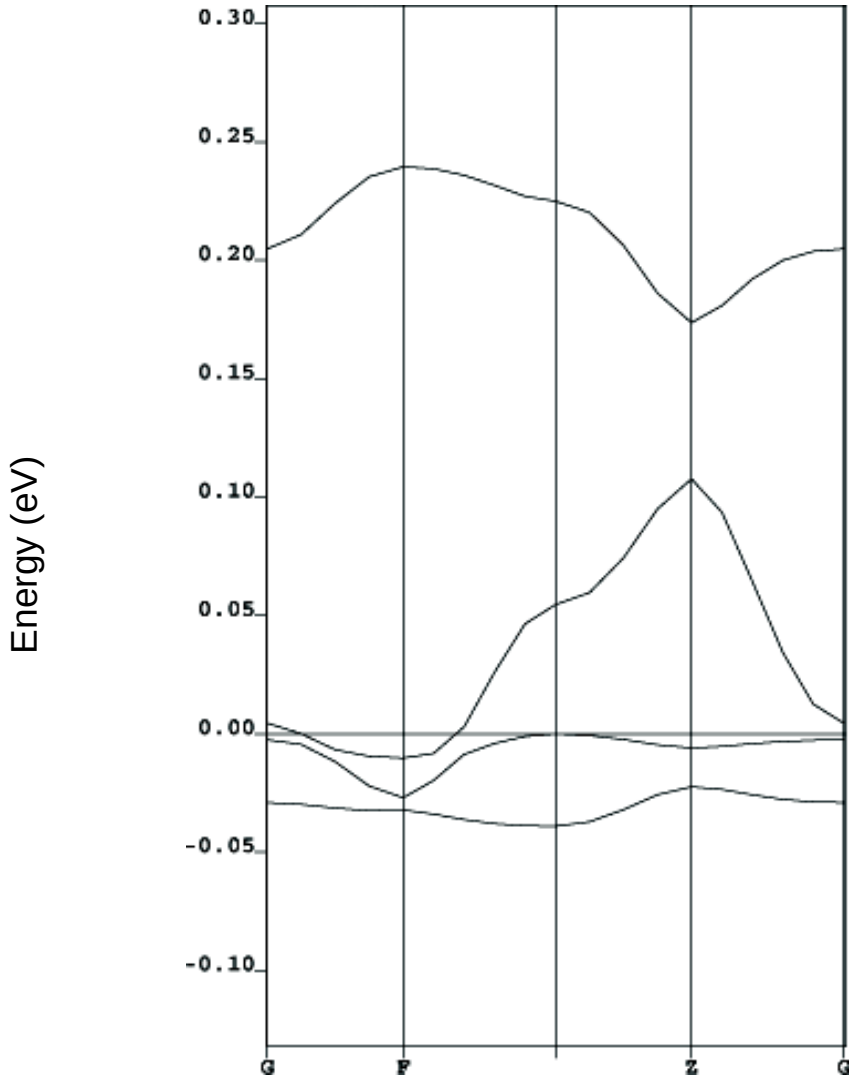


Figure 2. The band structure in the vicinity of the Fermi level of sheared TATB.

Intuitively, one would expect dramatic changes in the atomic and electronic properties of a heterogeneous molecular solid under a violent assault. One plausible mechanism is electronic excitation: electrons are light, fast and quantal, thus responding first to exterior perturbations. Following electronic excitation, however, several processes could be at play to induce chemical reactions. These include dissociation on the excited state surface, radiative processes, and nonradiative energy deactivation.

We have considered the topology of the ground and first excited states of the nitromethane molecule, [40] to investigate the feasibility of a nonradiative energy mechanism

following electronic excitation. The equilibrium geometry of the triplet state (the first electronically excited state) of the molecule is such that the ONO bond makes an angle of about 50 degree relative to the C-N bond, similar to nitro group bending in TATB that was discussed above (Fig.1). The equilibrium structure of the triplet state is thus markedly different form the equilibrium geometry of the ground singlet state where $\gamma$ is zero. An adiabatic barrier to dissociation on this first excited state with respect to the C-N bond was determined to be about 33 kcal/mol, using highly correlated ab initio multireference configuration interaction methodology. The existence of this barrier should presumably allow the triplet state to support a few vibrational levels, and owing to a different spin multiplicity that forbids decaying, to be long lived. Intersystem crossing, however, provides a nonradiative deactivation channel, and such a crossing has been located by determining the minimum energy crossing point (MECP) on the singlet-triplet surface of intersection. [30] This point is located 13 kcal/mol above the equilibrium geometry of the triplet state, thus establishing a second barrier for energy redistribution that is more than half of the adiabatic one. It is expected, therefore, that thermal activation along the nitro bending mode to permit efficient energy transfer from the triplet state to higher vibrational levels of the ground surface. There are no experimental measurements on the triplet formation for nitromethane, but a recent study on nitrobenzene showed that the triplet formation is very efficient with a quantum yield of $\geq$ 80%, and that this state has a lifetime of $\leq$ 500 ps. [41] An earlier experimental study established a very short nonradiative lifetime of about one picosecond for the excited singlet state of nitromethane, with efficiency of 76% in energy deactivation. [42] Vibrationaly hot ground-state molecules could thus be generated by fast internal conversion (singlet-singlet) and intersystem (singlet-triplet) crossings. The excess, nonradiative energy (heat) could presumably then be supplied to near shell molecules and speed up the decomposition process.

## 3. EFFECTS OF STATIC HIGH-PRESSURE

The effect of bending of the nitro group in TATB and nitromethane indicates *how* a band-gap closure can be achieved. The question remains, however, weather appreciable bending of the $NO_2$ group inside the crystal can be achieved within the experimentally accessible pressure range. This can be addressed through electronic structure calculations on the effect of static pressure, uniform and uniaxial, on the optical gap of nitromethane.

Briefly, the electronic structure calculations are based on the self-consistent charge density-functional tight binding (SCC-DFTB) scheme. [43] This is an extension of the standard tight binding approach [44] in the context of DFT, [45] and self-consistently describes total energies, atomic forces, and charge transfer. An essential element of our analysis is that, for each fixed set of lattice parameters, all interatomic positions are determined by total energy minimization, i.e., the atoms are fully relaxed. The tight-binding character of the SCC-DFTB makes it feasible to study large supercells, containing up to 32 molecules. The present study [46] compliments, with respect to computational tools and system sizes, an earlier first-principles calculations, which considered smaller supercells with more demanding and accurate first-principles computations. [31] The two methods give very similar results for the band gap of systems accessible to both.

To simulate the effect of uniform strain on solid nitromethane, the initial lattice parameters were successively decreased by keeping their ratio fixed. The pressure $P$ is estimated by using the low-temperature formula $P = \partial E_{tot} / \partial V$. For hydrostatic compression up to 50% of the original volume $V_0$ , the pressure rises to about 50 GPa, while the HOMO-LUMO gap dropped by 0.6 eV, i.e., by 13% of its original value. This compression results in a simultaneous increase of the HOMO and the LUMO energies, while the decrease of the HOMO-LUMO gap is almost monotonic in the volume strain, as depicted in Fig.3. The

change induced in the band gap by very high hydrostatic compression is shown in Fig.4 for strain equal up to 70%.

It is of interest to note that the mutual orientations of the C-N axes vary smoothly with the strain, $(V_0\text{-}V)/V_0$ , when this is less than 40%, with the corresponding pressure not exceeding 20 GPa. When $V/V_0$ is between 58% and 60% and $P$ is estimated to lie between 15 and 25 GPa, the atomic configuration undergoes an abrupt change accompanied by rotations of the methyl ($CH_3$) groups, in agreement with first-principles calculations; [31] a similar transition was observed in that work for $V/V_0$ between 59% and 77% and $P$ in the range 10-30 GPa. This transition is expected because the barrier for the rotation of the methyl group is known to be very low. [47]

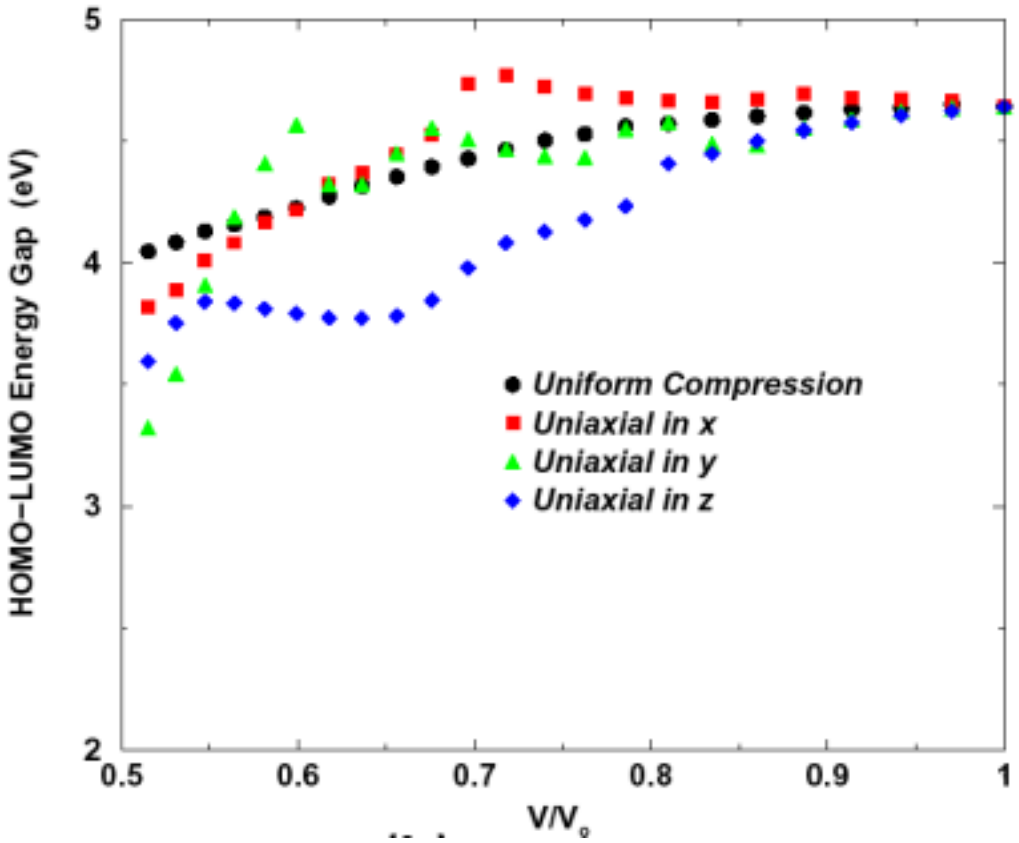


Fig.3. HUMO-LUMO energy gap of the prefect nitromethane crystal under uniform and uniaxial compression of the primitive unit cell.

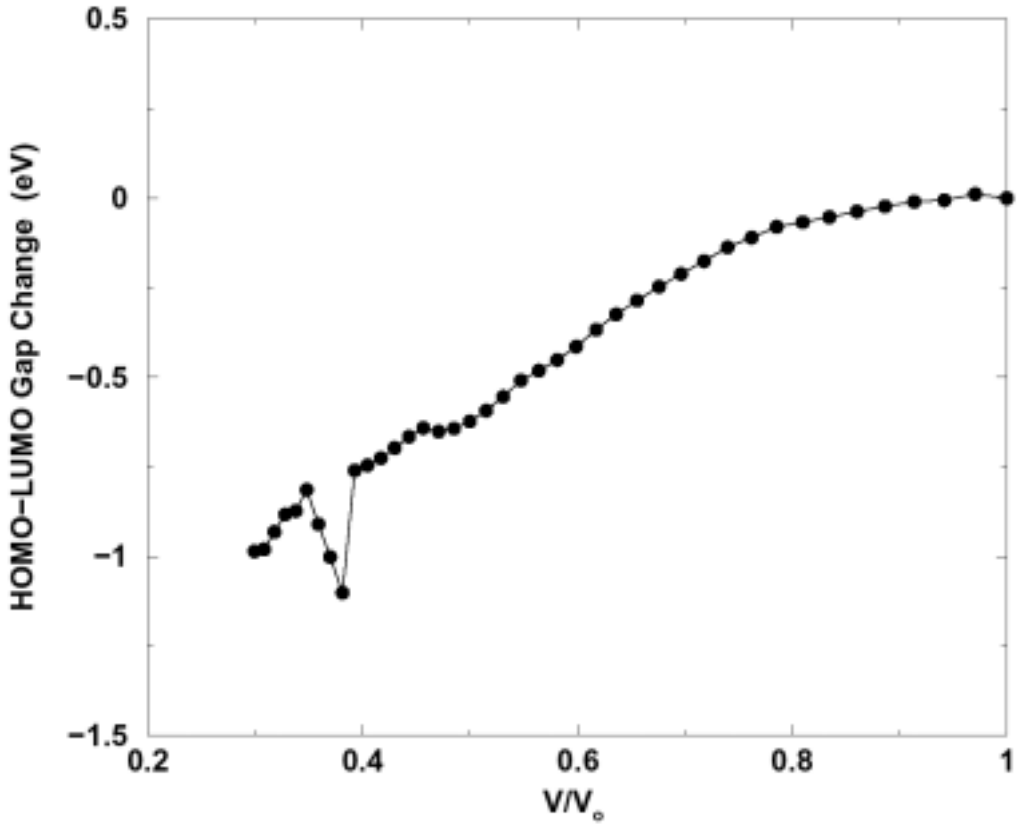


Fig.4. HUMO LUMO gap change under uniform compression. The sudden drop in the gap corresponds to the reported high C-H bond stretching.

The following changes of the bond lengths and bond angles were observed as the strain varied from 0 to 50%. While practically no bending of the nitro group in the molecules took place, the C-N bond lengths were invariably shortened at most by 6%. In contrast, the eight N-O bond lengths in the unit cell exhibited different variations, with a maximum

deviation of 61% from their equilibrium values. The bond angles involving the nitro group in each molecule remained practically intact. A few of the C-H bonds were stretched up to 2% of their initial values. No significant change in the bond angles involving the nitro group was noticed even as the uniform strain was increased from 50% to 70%. However, two of the C-H bonds were highly stretched when the strain was extended to values above 60%. The same effect on the C-H bond in all molecules of the unit cell was also observed under uniaxial stress, yet the estimated pressure is appreciably lower. This case is discussed in more detail below.

Compared to uniform compression, uniaxial strain along one of the lattice vectors is more likely to lead to detonation. Dick has proposed [48] that detonation initiation in nitromethane is favored by shock-wave propagation in specific directions related to the orientation-dependent steric hindrance to the shear flow. This proposal is based on a model according to which the sterically hindered shear process causes preferential excitation of optical phonons strongly coupled with vibrons.

We applied uniaxial compression along each of the *x, y*, and *z* axes, and tracked the HOMO-LUMO gap as a function of the volume change, for strains not exceeding 50% and corresponding estimated pressures as high as 100 GPa (see Fig. 3). Among the three types of compression, the ones in *x* and *y* yielded the highest estimated pressure. The gap was decreased at most by 1.4 eV (a 30% reduction of the original value) under stress in *y*. This drop is higher than in the case with uniform strain, while the gap behavior here is not strictly monotonic, i.e., the gap does not continuously decrease as the uniaxial strain increases. The strains in *x* and *y* seem to cause a similar overall behavior of the gap. The compression in *y*, however, causes a steeper reduction of the gap as $V/V_0$ approaches 50%. In contrast, the compression in *z* reduces the energy gap more drastically for intermediate values of $V/V_0$ ,

roughly between 65% and 80%. This last effect can be visualized as follows. The molecules approach each other in *z* by bringing the methyl group of one close to the nitro group of the next, while the cell lattice parameter *c* approaches the intermolecular distance. Consequently, the electron densities of the HOMO and the LUMO, which are localized near the nitro group, are distorted more than in any other type of compression of similar magnitude and the band gap is reduced more rapidly for this type of uniaxial strain.

A closer look at the atomic configurations reveals structural transitions which are triggered preferentially by pressure anisotropy. The most frequent transition in the *x* compression involves of course molecule translations, rotations of the methyl groups (which occur even for $V/V_0$ close to 1) and reorientations of the molecules, primarily via relative translations and rotations around their C-N axes. Two such abrupt transitions are observed when $V/V_0$ = 67-70% and the estimated pressure is 25-30 GPa, and $V/V_0$ = 59-62% with an estimated pressure of 45-55 GPa. In the *z* compression the methyl groups seem to undergo smoother transitions as each molecule's center-of-mass is translated in *z*. In contrast, the *y* compression causes abrupt transitions when $V/V_0$ = 76 81% and 63-66% and the pressure is estimated to lie in the ranges 2-5 and 13-16 GPa, respectively.

Notably, the dramatic stretching of four C-H bonds, one in each nitromethane molecule of the unit cell, occurs under stress in *y* when $V/V_0$ is between 59% and 62%, with an estimated pressure of 25-40 GPa; more precisely, these bond lengths are stretched by more than 10-12% of their original values in this case. The increase of strain in *y* above 50% causes these bonds to be stretched further and leads to the abstraction of their protons. This indication of proton dissociation corresponds to the steep part of the curve in Fig. 4, and renders the *y* and *x* compressions qualitatively different.

The C-N bond lengths are again invariably shortened, at most by 6%, 9%, and 2-3% of

their initial values under *x, y*, and *z* compression, respectively. In contrast, the N-O bond lengths exhibit positive or negative deviations from their equilibrium values that depend both on the location of the corresponding molecules and the direction of compression. It is worthwhile noting that only the compression in *y* causes the N-O bond length to be continuously stretched in all molecules at most by 3% of the initial value. The bond angles do not exhibit any change worthy of reporting for this range of compression.

As mentioned previously, the SCC-DFTB calculations predict a high stretching of the C-H bond that leads to proton abstraction under *y* compression when the strain becomes of the order of 40% or higher; for uniform compression, the corresponding strain takes the significantly higher values, in the range 60-62%, at estimated pressure of 150-180 GPa. One of the intermediate atomic configurations leading to the proton dissociation in the former case of uniaxial strain is shown in Fig.5. Note that the high stretching of the C-H bond is visualized graphically by enlarging the symbols that correspond to each abstracted acidic hydrogen atom (the atomic sizes in these figures are proportional to the van der Waals radius of the ionized form).

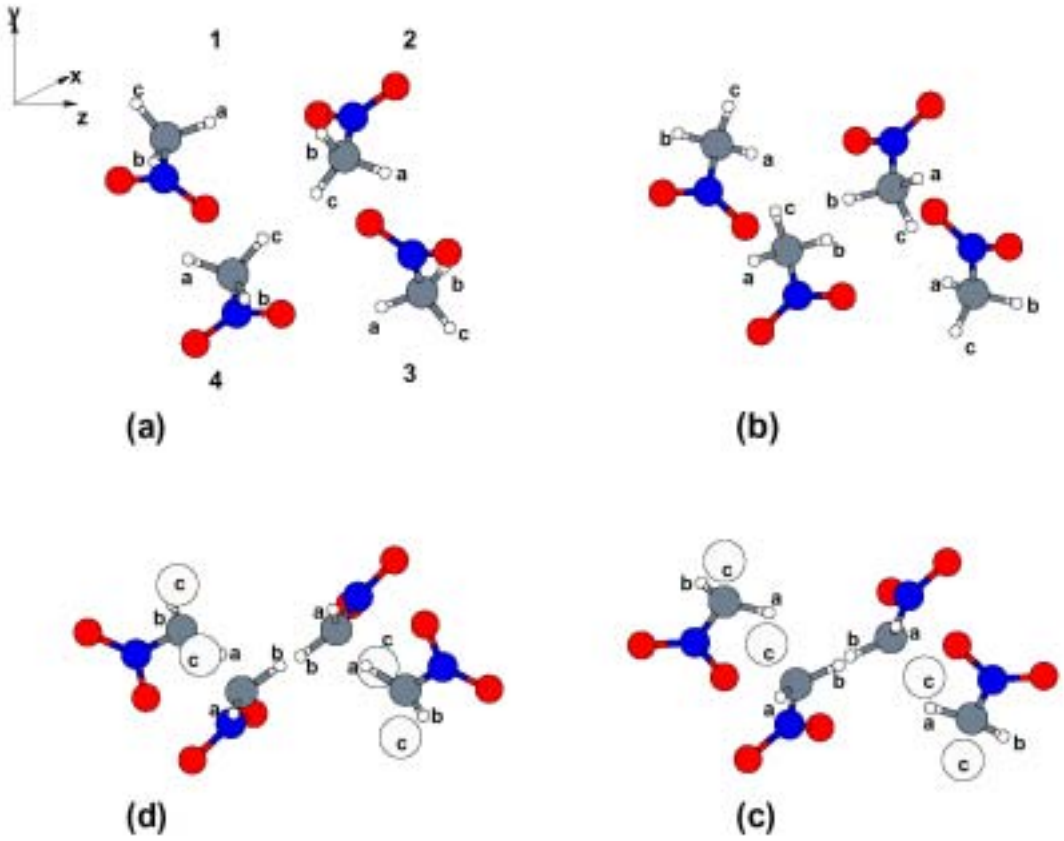


Fig.5. Atomic configurations of the unit cell for uniaxial compression along **b** direction, leading to H-abstraction. (a) Original cell at $V$ = 281.7 Å$^3$. (b) Molecular reorientation and methyl rotation at $V/V_0$ = 0.79. (c) C-H bond stretch by 12% at $V/V_0$ = 0.60. (d) Configuration at $V/V_0$ = 0.51. In (c) and (d) the abstracted protons are shown in larger circles.

A physical picture of the C-H bond stretching is the following: upon contraction of the initially single C-N covalent bond, electronic charge is transferred to the region of space between the C and N atoms. Consequently, the C-N bond becomes stronger and its character approaches that of a double covalent bond. The adjacent C-H bonds act as sources of the electronic charge; at least one of these H atoms is deprived of some electronic charge and its bond is weakened. On the other hand, the orbitals localized near the $NO_2$ group are not significantly distorted by the compression. The Mulliken charge changes given in Table 1 are

in agreement with this picture. The total Mulliken charge loss of the H atoms is found to increase monotonically with uniaxial strain in each molecule, being dominated for high strain by the charge pertaining to the markedly stretched C-H bonds (shown in Fig. 5), as expected. While these values follow closely the Mulliken charge gain of the C atoms for low uniaxial strain, they start to deviate significantly as the strain approaches 50%.

These findings imply that chemical reactions and transitions from covalent to ionic C-H bonds prior to detonation in nitromethane are more likely to start *before* the closure of the optical gap. A recent computational study [33] predicted a metallization pressure in TATB at 120 GPa, far above the detonation pressure. For the case of nitromethane, an actual precursor to detonation appears to be the proton dissociation. Interestingly, energetic materials can therefore be considered as more sensitive to their chemistry under uniaxial rather than uniform compression, in agreement with Dick's results that invoke a steric hindrance model for nitromethane. [48]

There have been numerous experimental studies of the reaction kinetics that may lead to detonation of liquid nitromethane. Most of these studies are concerned with the nature of chemical products that may speed up detonation. Shaw *et al.*, [49,50] for example, measured the effect of the concentration of protonated compounds within the energetic material on the time needed until explosion. Their experiments indicated that a reaction involving hydrogen atoms or protons is involved in the first steps of this fast-reaction process. This suggestion was later corroborated by Blais *et al.* [51] by more direct measurements, who also referred to a sequence of previous investigations by Engelke and co-workers. [52,53] Our zero-temperature, static calculations point to similar conclusions for the nitromethane molecular crystal. A similar prediction for this material was also reached concurrently via ongoing first principles, molecular-dynamics simulations at high densities (1.5-2.5 g/cm$^3$) and high temperatures ($T$ =

2000-4000 K). [54]

Table 1

Mulliken charges changes of carbon and hydrogen of the nitromethane molecules 1 and 2 in the unit cell under uniaxial compression along **b**.

| $V/V_0$ | $C_1$ | $H_{1a}$ | $H_{1b}$ | $H_{1c}$ | $C_2$ | $H_{2a}$ | $H_{2b}$ | $H_{2c}$ |
|---|---|---|---|---|---|---|---|---|
| 0.79 | 0.012 | -0.010 | 0.016 | 0.016 | 0.012 | -0.010 | 0.016 | 0.020 |
| 0.60 | 0.126 | -0.016 | -0.026 | -0.026 | 0.108 | -0.019 | -0.008 | -0.155 |
| 0.51 | 0.294 | -0.014 | -0.074 | -0.074 | 0.168 | -0.051 | -0.030 | -0.245 |

# 4. DECOMPOSITION KINETICS OF HMX

Detailed description of the chemical reaction mechanisms of condensed energetic materials at high densities and temperatures is essential for understanding events that occur at the reactive front of these materials under combustion or detonation conditions. Under shock conditions, for example, energetic materials undergo rapid heating to a few thousand degrees and are subjected to a compression of hundreds of kilobars, [55] resulting in almost 30% volume reduction. Complex chemical reactions are thus initiated, in turn releasing large amounts of energy to sustain the detonation process. Clearly, understanding of the various chemical events at these extreme conditions is essential in order to build predictive models of material properties that can be incorporated into fully-continuum approaches of describing the detonation process at the macroscopic level.

HMX (1,3,5, 7-tetranitro-1, 3,5,7-tetraazacyclooctane) is widely used as an ingredient in various explosives and propellants. A molecular solid at standard state, it has four known polymorphs, one of which, the δ phase is comprised of six molecules per unit cell. In a recent study, we have conducted a quantum-based molecular dynamics simulation of the chemistry of HMX under extreme conditions, similar to those encountered at the Chapman-Jouget detonation state. [16] The simulation studied the reactivity of dense (1.9 g/cm$^3$) fluid HMX at 3500K for extended reaction times of up to 55 picoseconds, thus allowing the formation of stable product molecules.

There are numerous experimental characterizations at low temperatures (i.e. < 1000 K, well below detonation temperature) of decomposition products of condensed-phase HMX. [56-68] These studies tend to identify final gas products (such as $H_2O$, $N_2$, $H_2$, CO, $CO_2$, etc.) from the surface burn, and aspire to establish a global decomposition mechanism. The early thermal decomposition study using mass spectrometry at T=503, 527, and 553 K of

Syryanarayana et al. [56] identified a concerted decomposition into four methylenenitramine ($CH_2N_2O_2$), which can further decompose into $CH_2O$ and $N_2O$. At 448-548 K, Farber and Srivastava [58] identified a major decomposition product with m/e=148 and proposed a homolytic cleavage of HMX to two $C_2H_4N_4O_4$ fragments that might further decompose to form methylenenitramine via $C_2H_4N_4O_4 \rightarrow 2\ CH_2N_2O_2$. $CH_2N$ and $NO_2$ were later detected as decomposition products from the $CH_2N_2O_2$ intermediate in an electron spin resonance pyrolysis study. [59] Recent experiments using thermogravimetric modulated beam mass spectrometry and isotope scrambling identified gaseous pyrolysis products such as $H_2O$, HCN, CO, $CH_2O$, NO, and $N_2O$ between 483 and 508 K. [61-63] Brill et al. have analyzed rate measurements for the early stage of HMX thermal decomposition, [65] revealing the existence of an approximate linear relationship between the Arrhenius prefactor, ln $A$, and the apparent activation energy, $E_a$. Brill later suggested two competing global mechanisms for thermal decomposition, the first leading to 4HONO and 4HCN, while the second leads to the formation of $4CH_2O$ and $4N_2O$. [66]

The above noted experimental work on thermal decomposition of condensed phase HMX is largely restricted to relatively low temperature (~550 K) and pressure (0.1 GPa) regimes. Similar experimental observations at detonation conditions (temperatures 2000-5000 K, and pressure 10-30 GPa), however, have not been realized to date. While recent applications of ultrafast spectroscopic methods [69] hold great promise for determining such decomposition mechanisms in the foreseeable future, at present, computer simulations provide the best access to the short time scale processes occurring in these regions of extreme conditions of pressure and temperature. [70] In particular, simulations employing many-body potentials, [17,71,72] or tight-binding based methods have emerged as viable computational tools, the latter has been successfully demonstrated in the studies of shocked hydrocarbons. [14,15]

Previous theoretical studies have included electronic structure calculations of various decomposition channels of the gas-phase HMX molecule. [73-75] Melius used the Bond-Additivity-Corrected (BAC) MP4 method to determine decomposition pathways for nitramine compounds, HMX and RDX. [73] The initial step in his decomposition scheme is N-$NO_2$ bond breaking, which subsequently causes a significant weakness in the second-nearest-neighbor bond breaking energies (18 kcal/mol for the C-N bond dissociation), leading to HCN, $NO_2$, and H as the net products for rapid thermal heating. In the condensed phase, however, Melius made the observation that alternative decomposition mechanisms can occur. The deposed $NO_2$ fragment can recombine as a nitride, which an then decompose by breaking the O-N bond to form NO, or attract weakly hydrogen atoms and form HONO. The HONO molecules can then rapidly equilibrate to form water via the reaction $2HONO \rightarrow H_2O + NO_2 + NO$.

Lewis et al. [74] calculated four possible decomposition pathways of the a-HMX polymorph: N-$NO_2$ bond dissociation, HONO elimination, C-N bond scission, and the concerted ring fission. Based on the energetics, it was determined that N-$NO_2$ dissociation was the initial mechanism of decomposition in the gas phase, while they proposed HONO elimination and C-N bond scission to be favorable in the condensed phase. The more recent study of Chakraborty et al. [75], using the DFT(B3LYP) method, reported detailed decomposition pathways of the b-HMX, the stable polymorph at room temperature. It was concluded that consecutive HONO elimination (4HONO) and subsequent decomposition into HCN, OH and NO are energetically the most favorable pathways in the gas phase. The results also showed that the formation of $CH_2O$ and $N_2O$ could occur preferably from secondary decomposition of methylenenitramine. While these studies concentrated on gas phase decomposition mechanisms, to date no computational treatment of condensed phase reaction mechanisms exist. Other theoretical studies were concerned with the derivation of a

force field from first principle calculations, [76] and the application of classical molecular dynamics as in simulating pressure effects on crystal packing. [77,78]

The computational approach to simulate the condensed-phase chemical reactivity of HMX is based on implementing the self-consistent charge density-functional tight binding (SCC-DFTB) scheme. [43] The initial condition of the simulation included six HMX molecules in a cell, corresponding to the unit cell of the d phase of HMX with a total of 168 atoms. It is well known [79] that HMX undergoes a phase transition at 436 K from the b phase (two molecules per unit cell with a chair molecular conformation, density = 1.89 g/cm$^3$) to the δ phase (with boat molecular conformation, density=1.50 g/cm$^3$). The δ phase was thus chosen as the initial starting structure so as to include all the relevant physical attributes of the system prior to chemical decomposition. The calculation started with the experimental unit cell parameters and atomic positions of δ HMX. The atomic positions were then relaxed in an energy minimization procedure, and were verified to be close to the experimental positions.

The volume of the cell was then reduced to the final density of the simulation. The atomic structure was subsequently fully optimised at the corresponding cell volume. Since the purpose of the simulation is to study the high- pressure and high- temperature chemistry of HMX in general, the exact density and temperature used in our simulation is somewhat arbitrary. The density of 1.9 g/cm$^3$ and a temperature of 3500 K were chosen. This state is in the neighborhood of the Chapman-Jouget state of β-HMX (3500 K, 2.1g/ cm$^3$) as predicted through thermochemical calculations described later. The closest experimental condition corresponding to this simulation would be a sample of HMX, which is suddenly heated under constant volume conditions, such as in a diamond anvil cell.

The molecular dynamics simulation was conducted at constant volume and constant temperature. Periodic boundary conditions, whereby a particle exiting the cell on one side is

reintroduced on the opposing side with the same velocity were imposed. Constant temperature conditions were implemented through simple velocity rescaling. The probability to rescale atom velocities was chosen to be 0.1 per time step. A dynamic time-step of 0.5 fs was used, and snapshots at 2.5 fs steps were collected.

A procedure was implemented to identify the product molecules of interest: $H_2O$, $N_2$, $CO_2$, and CO. Covalent bonds were identified according to bond distance. This is motivated by the difference between covalent (1 - 1.7 Å) and van der Waals bond distances (~3 Å). Maximum bond distances of: R (O-H)=1.3, R (CO)=1.7, and R(N-N)=1.5 Å were chosen in the molecule identification procedure. Since transition states are short lived, this problem should not significantly affect the reported time averaged concentrations of the species.

Under the simulation conditions, the HMX was in a highly reactive dense fluid phase. There are important differences between the dense fluid (supercritical) phase and the solid phase, which is stable at standard conditions. Namely, the dense fluid phase cannot accommodate long-lived voids, bubbles, or other static defects. Instead numerous fluctuations in the local environment occur within a timescale of 10s of femtoseconds. The fast reactivity of the dense fluid phase and the short spatial coherence length make it well suited for molecular dynamics study with a finite system for a limited period of time. Under the simulation conditions chemical reactions occurred within 50 fs. Stable molecular species were formed in less than one picosecond. Figs. 6 (a-d) display the product formation of $H_2O$, $N_2$, $CO_2$ and CO, respectively. The concentration, $C(t)$, is represented by the actual number of product molecules formed at the corresponding time $t$. Each point on the graphs (open circles) represents a 250 fs averaged interval. The number of the molecules in the simulation was sufficient to capture clear trends in the chemical composition of the species studied. These concentrations were in turn fit to an expression of the form: $C(t) = C_\infty(1- e^{-bt})$, where $C_\infty$

is the equilibrium concentration and b is the effective rate constant. From this fit to the data, we estimate effective reaction rates for the formation of $H_2O$, $N_2$, $CO_2$, and CO to be 0.48, 0.08, 0.05, and 0.11 $ps^{-1}$, respectively.

It is not surprising that the rate of $H_2O$ formation is much faster than that of $N_2$. Fewer reaction steps are required to produce a triatomic species like water, while the formation of $N_2$ involves a much more complicated mechanism. [73] Further, the formation of water (Fig.1-a) starts around 0.5 ps and seems to have reached a steady state at 10 ps, with oscillatory behavior of decomposition and formation clearly visible. The formation of $N_2$ (Fig.1-b), on the other hand, starts around 1.5 ps and is still progressing (slope of the graph is slightly positive) after 55 ps of simulation time, albeit at small variation.

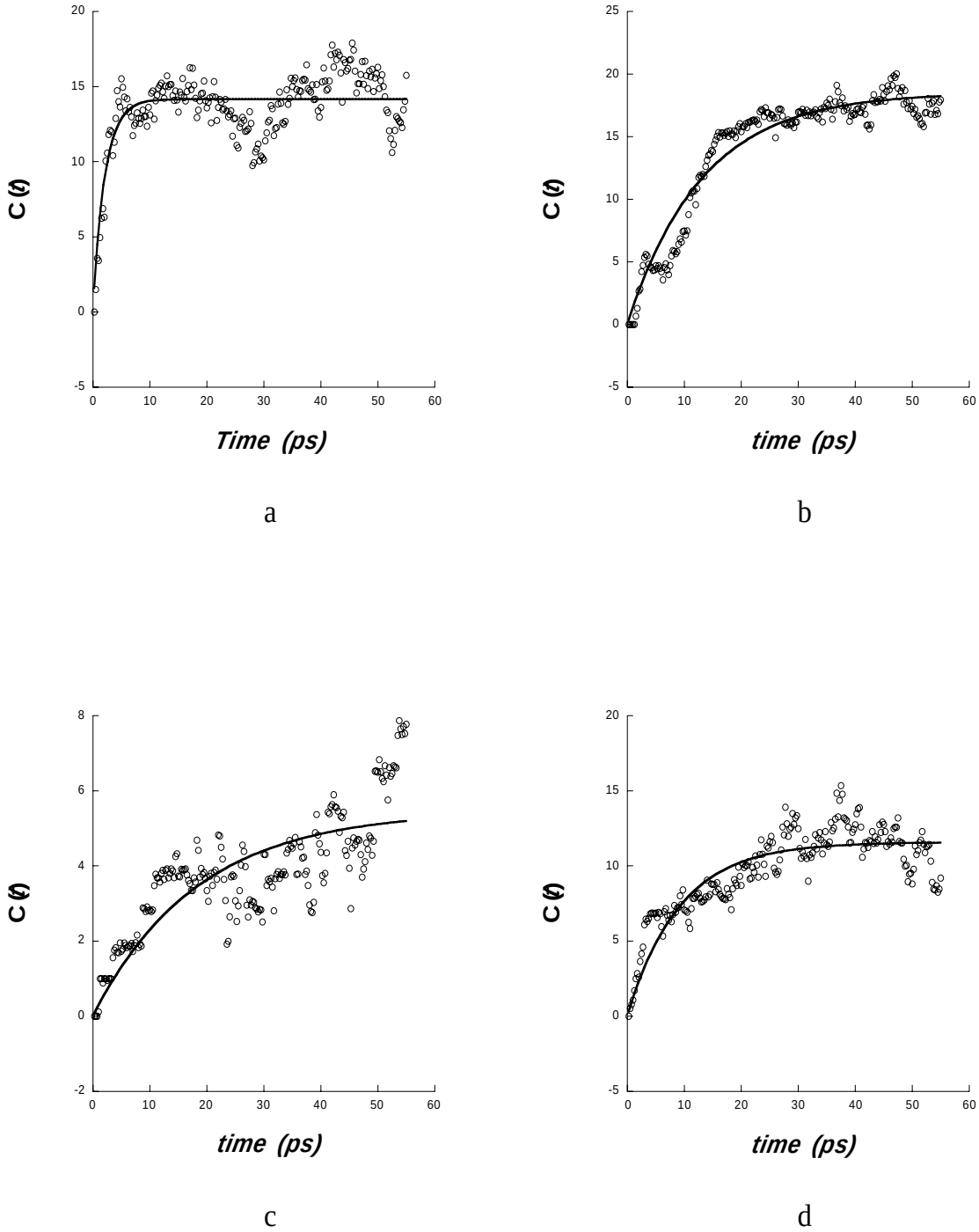


Fig. 6. Product particle-number formations as a function of time of (a) $H_2O$, (b) $N_2$, (c) $CO_2$, and (d) CO.

Due to the lack of high-pressure experimental reaction rate data for this (and other) explosive(s) with which to compare with, we produce in Fig.7 a comparison of dominant species formation for decomposing HMX obtained from entirely different theoretical approach. The concentration of species at chemical equilibrium can be estimated through thermodynamic calculations, as implemented within the Cheetah thermochemical code. [80,81] For HMX, the molecules $N_2$, $H_2O$, $CO_2$, HNCO, and CO were predicted to be present in quantities greater than 1 mol/kg HMX. The species CO, $NH_3$, $H_2$, $CH_4$, H, $CH_3OH$, NO, and $C_2H_4$ were also predicted to be present in quantities greater than 0.0001 mol/kg HMX. The species $N_2O$, $C_2H_2$, N, O, $O_2$, $NO_2$, HCN, atomic C, and $O_3$ were not predicted to have significant concentrations. Carbon in the diamond phase was predicted to be in equilibrium with the other species at a concentration of 4.9 mol/kg HMX. The thermochemical calculations predict a pressure for fully reacted HMX of 16 GPa, or 160 kBar.

As can be noticed in Fig.7, the results of the MD simulation compare very well with the formation of $H_2O$, $N_2$, and HNCO. The relative concentration of CO and $CO_2$, however, is reversed at the limited time of the simulation. No condensed carbon was found in the current simulation. Several other products and intermediates with lower concentrations, common to the two methods, have also been identified. These include HCN, $NH_3$, $N_2O$, $CH_3OH$, and $CH_2O$. It is hoped that interplay between the two vastly different approaches could be established at much longer simulation time. The goal will be to expand the product molecule set of the theromochemical code with important species determined from our ab nitio based simulations for kinetic modelling.

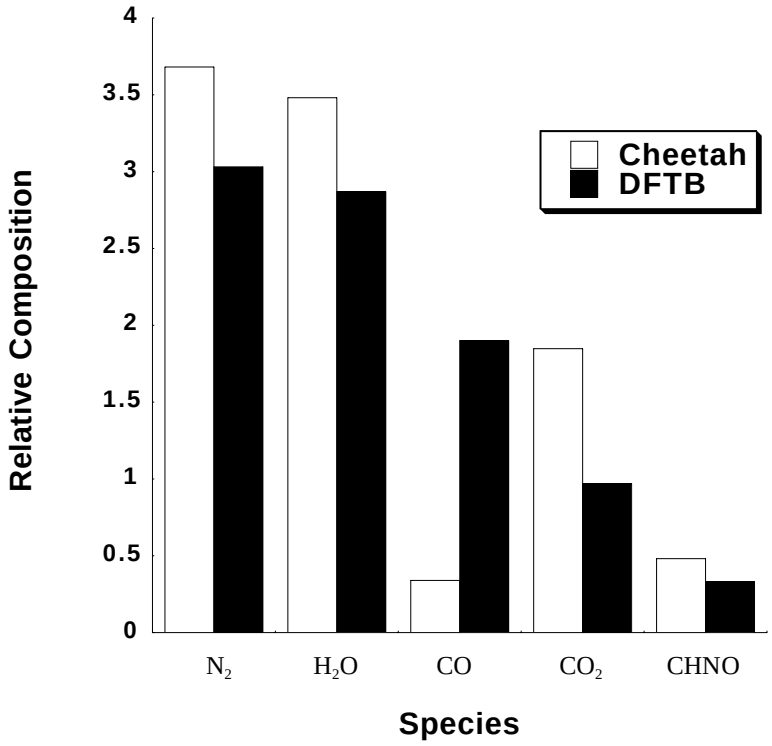


Fig.7. Comparison of relative composition of dominant species determined from current DFTB simulation and from a thermodynamical calculation.

One expects more $CO_2$ than CO as final products, as predicted by Cheetah (Fig.7). The results displayed in Figs.6 (c-d) show that, at simulation time of 40 ps, the system is still in the second stage of reaction chemistry. At this stage, the CO concentration is rising and has not yet undergone the water gas shift reaction ($CO + H_2O \rightarrow CO_2 + H_2$) conversion. Interestingly, this shift seems to occur at around 50 ps of the simulation, with $CO_2$ molecules are being formed while CO concentration is correspondingly diminishing.

The current simulation should allow for the construct of a global reaction mechanism for the decomposition of HMX at the stated physical conditions. Here, the initial steps of the decomposition pathways are considered. The first chemical event in the simulation is the

breaking of the N-$NO_2$ bond and the dissociation of $NO_2$ fragments. At 200 fs of simulation time, the number of $NO_2$ fragments is 10, out of a possible total of 24, with some being successive elimination from the same HMX molecule. This preference to bond rupture is consistent with the recent observation that the energetic barriers for the cleavage of N-$NO_2$ bond in the solid phase of the nitramine RDX vary depending on the location of the molecule in the crystal. [82] At this stage of the simulation, the C-N bond breaking is also exhibited, occurring in two ways: the first (1) producing methylenenitramine ($CH_2N_2O_2$), while the symmetric breaking (2) leads to the formation of two $C_2H_4N_4O_4$ moieties, as shown below.

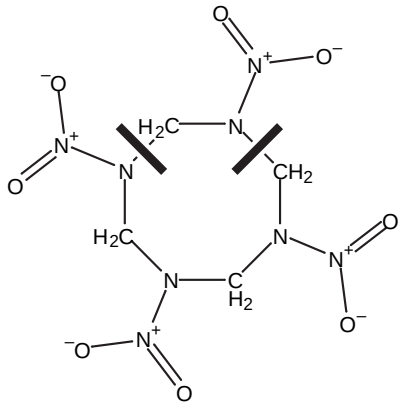

(1)

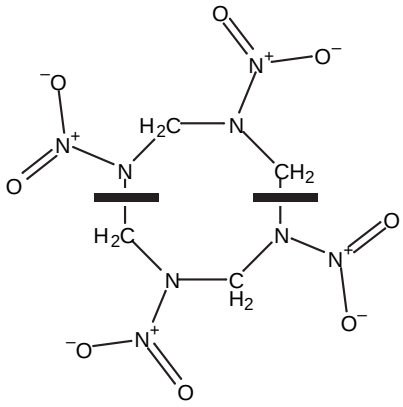

(2)

Seven $CH_2N_2O_2$ species have been formed at around 200 fs of simulation time. These results are similar to those identified in thermal decomposition experiments. [56,58] A further N-$NO_2$ bond breaking then follows the decomposition (1) and (2) above. From (1), this leads to the formation of $CH_2N$ and $NO_2$. These pathways are remarkably similar to those predicted previously by Melius from the decomposition of nitramines at fast heating rates. [73]

As the radical $CH_2N$ is formed, the production of HCN occurs via the reaction:

$$CH_2N + CH_2N \rightarrow C_2H_4N_2 \rightarrow HCN + CH_2NH.$$

Another source for the formation of HCN follows from a series of complex reactions that also produce nitric acid, $HNO_3$:

$$CH_2NH + NO_2 \rightarrow CH_3N_2O_2$$

$$CH_3N_2O_2 + NO_2 \rightarrow CH_2N_2O_3 + HNO$$

$$CH_2N_2O_3 \rightarrow HCN + HNO_3.$$

The schematic mechanism for these reactions is illustrated in Fig.8. It should be noted that formaldehyde, $CH_2O$, is first formed from a reaction involving large intermediate fragments. The formation occurs from the reaction of the $C_2H_4N_4O_4$ moiety, which is produced from the symmetric bond scission of the HMX molecule as in (2) above, with HNO. The reaction leads to the production of $CH_2O$ and a larger intermediate fragment that undergoes further decomposition.

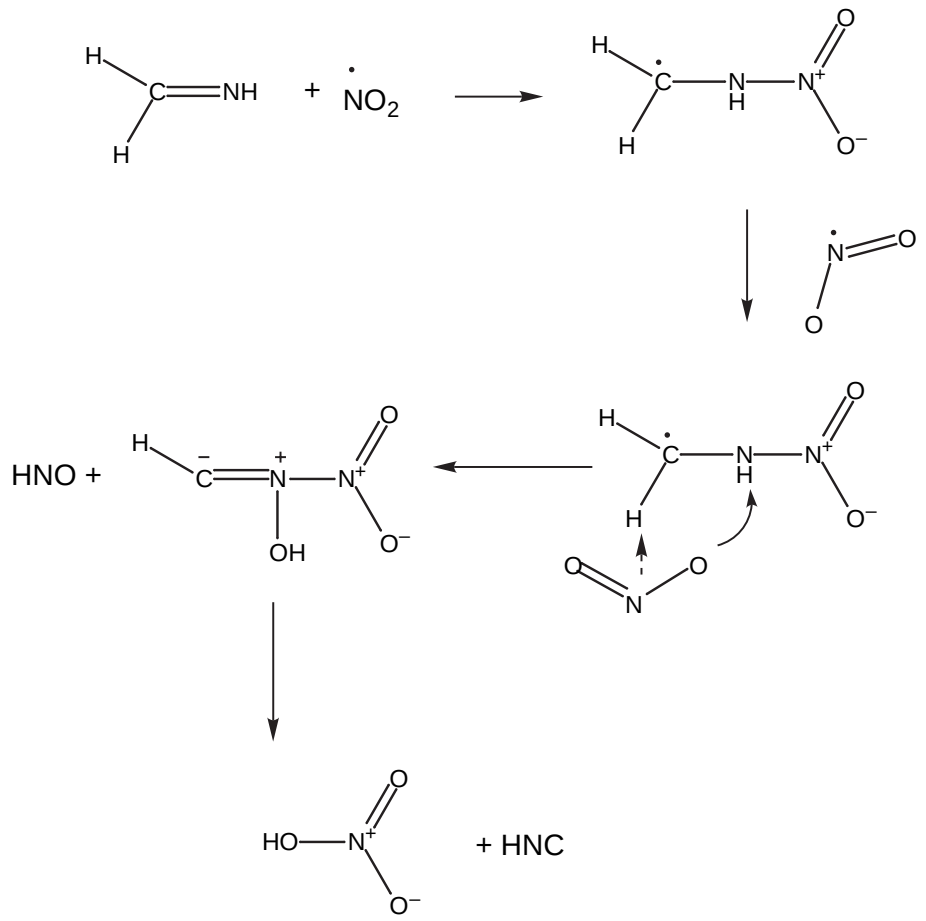


Fig.8. Mechanistic scheme for the formation of HCN.

Although the simulation sheds light on the chemistry of HMX under extreme conditions, there are methodological shortcomings that need to be overcome in the future. The demanding computational requirements of the present method limits the method's applicability to short times and corresponding high temperature conditions. A second issue is that the SCC-DFTB method is not as accurate as more elaborate ab initio methods. The high temperature condition of the simulation ameliorates this difficulty. For instance, at 3500K a 10 kcal/mol error in a reaction barrier leads to a factor of 4 error in the reaction rate. This is an acceptable error for a qualitative study. At 600K, however, a comparable error in the barrier would lead to a factor of 4000 in the reaction rate. Nonetheless, the present approach

could still be considered as a promising direction for future research on the chemistry of energetic materials.

## 5. MULTI-SCALE MODELING SHOCKED ENERGETIC MATERIALS

Study of the propagation of shock waves in condensed matter has led to new discoveries ranging from new metastable states of carbon [83] to the metallic conductivity of hydrogen in Jupiter, [84,85] but progress in understanding the microscopic details of shocked materials has been extremely difficult. Highly non-equilibrium regions may exist that give rise to the formation of unexpected metastable states of matter and determine the structure, instabilities, and time-evolution of the shock wave [86,87] Some progress in understanding these microscopic details can be made through molecular dynamics simulations. [15,88-90] The popular non-equilibrium molecular dynamics (NEMD) approach to atomistic simulations of shock compression involves creating a shock on one edge of a large system and allowing it to propagate until it reaches the other side. The computational work required by NEMD scales at least quadratically in the evolution time because larger systems are needed for longer simulations. When quantum mechanical methods with poor scaling of computational effort with system size are employed, this approach to shock simulations rapidly becomes impossible. Another approach that utilizes a computational cell moving at the shock speed has the same drawbacks. [91]

Recently, we presented a method that circumvents these difficulties by requiring simulation only of a small part of the entire system. [92] The effects of the shock wave passing through this small piece of the system are simulated by dynamically regulating the applied stress which is obtained from a continuum theory description of the shock wave structure. Because the size of the molecular dynamics system is independent of the simulation time in

this approach, the computational work required to simulate a shocked system is nearly linear in the simulation time, circumventing the scaling problems of NEMD.

Molecular dynamics simulations have been performed that utilize a shock Hugoniot-based thermodynamic constraint for the temperature at fixed volume. [93] Our proposed method enables the *dynamical* simulation of shock waves in systems that have material instabilities which lead to the formation of multiple shock waves and chemical reactions that can change the speed of shock propagation with time. It is a tractable method that requires no *a priori* knowledge of the system phase diagram, metastable states, or sound speeds.

To simulate a single shock wave, the propagation of the shock wave is modeled using the 1D Euler equations for compressible flow, which neglect thermal transport. These equations represent the conservation of mass, momentum, and energy respectively everywhere in the wave. Neglecting thermal transport in high temperature shocks is valid in systems where electronic mechanisms of heat conduction are not important, i.e. usually less than a few thousand K in insulators. [55] While the Euler equations are not rigorously applicable at elastic shock fronts, which can be atomistically sharp, the correct dynamics will be approximated in these special regions. We seek solutions of these equations which are steady in the frame of the shock wave moving at speed $\mathrm{v}_s$ by making the substitution $(x,t) \to x - \mathrm{v}_s t$. This substitution, and integration over $x$ yields a variation of the Hugoniot relations,

$$u = \mathrm{v}_s\left(1 - \frac{\rho_0}{\rho}\right) \tag{1}$$

$$p - p_0 = \mathrm{v}_s^2 \rho_0 \left(1 - \frac{\rho_0}{\rho}\right) \tag{2}$$

$$\epsilon - \epsilon_0 = p_0\left(\frac{1}{\rho_0} - \frac{1}{\rho}\right) + \frac{v_s^2}{2}\left(1 - \frac{\rho_0}{\rho}\right)^2 \qquad (3)$$

Here $u$ is the local speed of the material in the laboratory frame (particle velocity), $v$ is the specific volume, $\rho = \frac{1}{v}$ is the density, $\epsilon$ is the energy per unit mass, and $p$ is the negative component of the stress tensor in the direction of shock propagation, $-\sigma_{xx}$. Variables with subscripts 0 are the values before the shock wave, and we have chosen $u_0 = 0$ i.e. the material is initially at rest in the laboratory frame. In the language of shock physics, Eq. 2 for the pressure is the Rayleigh line and Eq. 3 for the internal energy is the Hugoniot at constant shock velocity. These equations apply to a system which has a time-independent steady-state in the reference frame moving at the shock speed $v_s$.

For the molecular dynamics simulation, we employ the Lagrangian,

$$L = T\left(\{\dot{\vec{r}}_i\}\right) - V\left(\{\vec{r}_i\}\right) + \frac{1}{2}Q\dot{v}^2 + \frac{1}{2}\frac{v_s^2}{v_0^2}(v_0 - v)^2 + p_0(v_0 - v) \qquad (4)$$

where $T$ and $V$ are kinetic and potential energies per unit mass, and $Q$ is a mass-like parameter for the simulation cell size. It can be seen that Eq. 4 in Hamiltonian form implies Eq. 3 when $\dot{v} = 0$ because $T + V = \epsilon$. The equation of motion for the system volume is,

$$Q\ddot{v} = \frac{\partial T}{\partial v} - \frac{\partial V}{\partial v} - p_0 - \frac{v_s^2}{v_0^2}(v_0 - v) \qquad (5)$$

which reduces to Eq. 2 when $\ddot{v} = 0$. The scaled atomic coordinate scheme is used to deal with the variable computational cell size. [94] This scheme introduces a volume dependence for $T$ and $V$. Strain is only allowed in the shock direction, i.e. $v_0 - v = -\varepsilon_{xx} v_0$ where $\varepsilon_{xx}$ is the

uniaxial strain. The pressures in Eq. 5, including the thermal contribution, are taken to be the uniaxial $x$ component of stresses. Computational cell dimensions transverse to the shock direction are fixed, as in NEMD simulations. This approach allows the simulation of shocks propagating in any desired direction.

Simulating a single shock wave may be accomplished by dynamically varying the uniaxial strain of the system according to Eq. 5. By choosing a small representative sample of the shocked material, it is assumed that stress gradients and thermal gradients in the actual shock wave are negligible on the length scale of the sample size. While the thermal energy is assumed to be evenly distributed throughout the sample, thermal equilibrium is not required. The simulated waves can be shown to obey the shock wave stability conditions, [92] which require $v_s > c_0$ in front of the shock wave and $u_1 + c_1 > v_s$ behind the shock, where $c$ is the local sound speed.

As a case study, we apply this method to nitromethane, experiencing a shock speed of 7 km/s. The atomic energies and forces were computed using the SCC-DFTB method, utilizing one unit cell of solid nitromethane. The dynamics were followed up 17.5 ps. Figure 9 shows the time profile of the density, stress, and temperature of the system throughout the simulation. Examination of the chemical events, we report the formation of $CH_2NO_2H$ moiety at about 7 ps in the simulation, persisting up for about 2 ps.

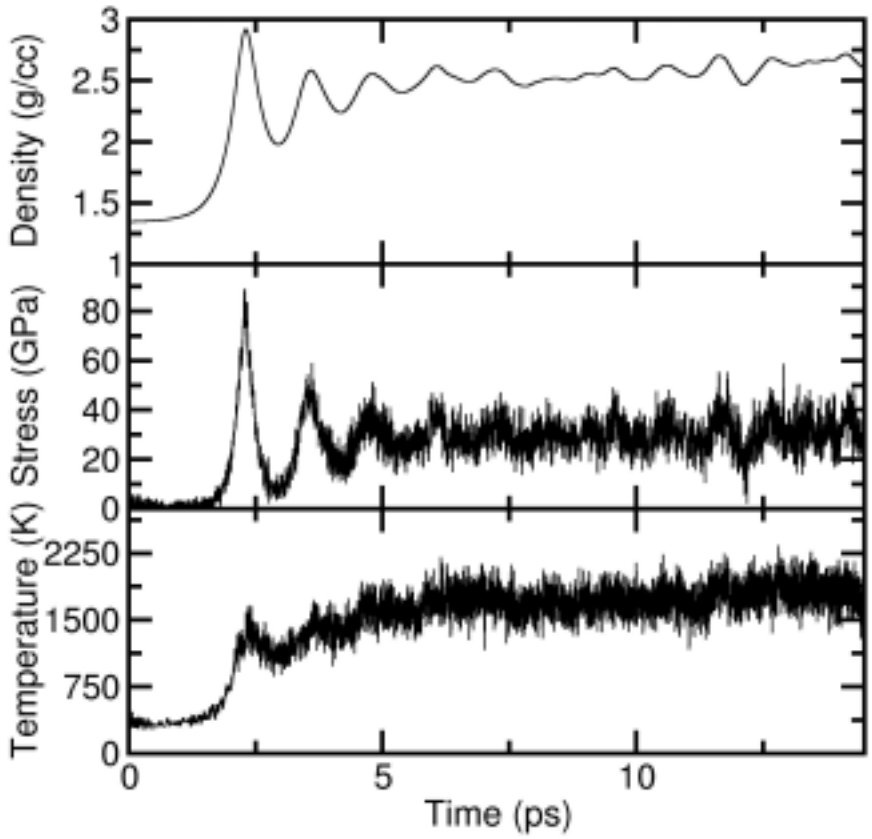


Figure 9. Temporal profile of the density, pressure, and temperature of shocked nitromethane.

## REFERENCES


1 A. W. Campbell, W. C. Davis, J. B. Ramsay, and J. R. Travis, *Phys. Fluids* **4,** 511 (1961).

2 N. S. Enikolopyan, *Dokl. Akad. Nauk SSSR* **283,** 612 (1985).

3 M. H. Miles and J. T. Dickinson, *Appl. Phys. Lett.* **41,** 924 (1982).

4 A. N. Dremin, S. D. Savrov, V. S. Trofimov, and K. K. Shvedov, *Detonation Waves in Condensed Matter* (Nauka, Moscow, 1970).

5 W. L. Elban, R. W. Armstrong, K. C. Yoo, R. G. Rosemeier, and R. Y. Yee, *J. Mater.Sci* **24,** 1273 (1989).

6 G. I. Kanel, S. V. Razorenov, A. V. Utkin, and V. E. Fortov, *Impact-Wave Phenomena in Condensed Matter* (Yanus-K, Moscow, 1996).

7 C. M. Tarver, S. K. Chidester, and A. L. Nichols III, *J. Phys. Chem.* **100,** 5794 (1996).

8 F. P. Bowden and A. D. Yoffe, *Initiation and rowth of Explosion in Liquids and Solids* (Cambridge University Press, London, 1952).

9 D. D. Dlott and M. D. Fayer, *J. Chem. Phys.* **92,** 3798 (1990).

10 C. S. Coffey, *Phys. Rev. B* **24,** 6984 (1981).

11 L. E. Fried, M. R. Manaa, P. F. Pagoria, and R. L. Simpson, *Annu. Rev. Mater. Res.* **31,** 291 (2001).

12 C. Cavazzoni, G. L. Chiarotti, S. Scandolo, E. Tosatti, M. Bernasconi, and M. Parrinello, *Science* **283,** 44 (1999).

13 F. Ancilotto, G. L. Chiarotti, S. Scandolo, and E. Tosatti, *Science* **275,** 1288 (1997).

14 S. R. Bickham, J. D. Kress, and L. A. Collins, *J. Chem. Phys.* **112,** 9695 (2000).

15 J. D. Kress, S. R. Bickham, L. A. Collins, B. L. Holian, and S. Goedecker, *Phys. Rev. Lett.* **83,** 3896 (1999).

16 M. R. Manaa, L. E. Fried, C. F. Melius, M. Elstner, and T. Frauenheim, *J. Phys. Chem. A* **106,** 9024 (2002).

17 M. L. Elert, S. V. Zybin, and C. T. White, *J. Chem. Phys.* **118,** 9795 (2003).

18 A. Strachan, A. C. T. van Duin, D. Chakraborty, S. Dasgupta, and W. A. Goddard, *Phys. Rev. Lett.* **91,** 098301 (2003).

19 C. S. Coffey, *Phys. Rev. B* **32,** 5335 (1984).

20 C. S. Coffey, *J. Appl. Phys.* **70,** 4248 (1991).

21 L. E. Fried and A. J. Ruggiero, *J. Phys. Chem.* **98,** 9786 (1994).

22 C. M. Tarver, *J. Phys. Chem. A* **101,** 4845 (1997).

23 C. M. Tarver, *Combust. Flame* **46,** 111 (1982).

24 C. M. Tarver, *Combust. Flame* **46,** 135 (1982).

25 C. M. Tarver, *Combust. Flame* **46,** 157 (1982).

26 J. J. Gilman, *Phil. Mag. B* **71,** 1057 (1995).

27 J. J. Gillman, *Philos. Mag. B* **67,** 207 (1993).

28 J. Sharma, B. C. Beard, and M. Chaykovsky, *J. Phys. Chem.* **95,** 1209 (1991).

29 M. R. Manaa, *Appl. Phys. Lett.* **83,** 1352 (2003).

30 M. R. Manaa and L. E. Fried, *J. Phys. Chem. A* **103,** 9349 (1999).

31 E. J. Reed, J. D. Joannopoulos, and L. E. Fried, *Phys. Rev. B* **62,** 16500 (2000).

[32] D. Margetis, E. Kaxiras, M. Elstner, T. Frauenheim, and M. R. Manaa, *J. Chem. Phys.* **117,** 788 (2002).

[33] C. J. Wu, L. H. Yang, L. E. Fried, J. Quenneville, and T. J. Martinez, *Phys. Rev. B* **67,** 235101 (2003).

[34] M. M. Kuklja and A. B. Kunz, *J. Phys. Chem. B* **103,** 8427 (1999).

[35] M. M. Kuklja and A. B. Kunz, *J. Appl. Phys.* **86,** 4428 (1999).

[36] M. M. Kuklja and A. B. Kunz, *J. Appl. Phys.* **87,** 2215 (2000).

[37] M. M. Kuklja and A. B. Kunz, *J. Phys. Chem. Solids* **61,** 35 (2000).

[38] M. M. Kuklja and A. B. Kunz, *J. Appl. Phys.* **89,** 4962 (2001).

[39] M. M. Kuklja, E. V. Stefanovich, and A. B. Kunz, *J. Chem. Phys.* **112,** 3417-3423 (2000).

[40] M. R. Manaa and L. E. Fried, *J. Phys. Chem. A* **102,** 9884 (1998).

[41] M. Takezaki, N. Hirota, and M. Terazima, *J. Phys. Chem. A* **101,** 3443 (1997).

[42] C. Rajchenbac, J. Gediminas, and C. Rulliere, *Chem.Phys.Lett.* **231,** 467 (1995).

[43] M. Elstner, D. Porezag, G. Jungnickel, J. Elsner, M. Hauk, T. Frauenheim, S. Suhai, and G. Seifert, *Phys. Rev. B* **58,** 7260 (1998).

[44] J. C. Slater and G. F. Koster, *Phys. Rev.* **94,** 1498 (1954).

[45] P. Hohenberg and W. Kohn, *Phys. Rev.* **136,** B864 (1964).

[46] D. Margetis, E. Kaxiras, M. Elstner, T. Frauenheim, and M. R. Manaa, *J. Chem. Phys.* **117,** 788 (2002).

[47] S. F. Trevino and W. H. Rymes, *J. Chem. Phys.* **73,** 3001 (1980).

[48] J. J. Dick, *J. Phys. Chem.* **97,** 6193 (1993).

[49] R. Shaw, P. S. Decarli, D. S. Ross, E. L. Lee, and H. D. Stromberg, *Combust. Flame* **35,** 237 (1979).

[50] R. Shaw, P. S. Decarli, D. S. Ross, E. L. Lee, and H. D. Stromberg, *Combust. Flame* **50,** 123 (1983).

[51] N. C. Blais, R. Engelke, and S. A. Sheffield, *J. Phys. Chem. A* **101,** 8285-8295 (1997).

[52] R. Engelke, W. L. Earl, and C. M. Rohlfing, *J. Phys. Chem.* **90,** 545 (1986).

[53] R. Engelke, D. Schiferl, C. B. Storm, and W. L. Earl, *J. Phys. Chem.* **92,** 6815 (1988).

[54] M. R. Manaa, E. J. Reed, L. E. Fried, G. Galli, and F. Gygi, *To be submitted* .

[55] Y. B. Zel'dovich and Y. P. Raiser, *Physics of Shockwaves and High Temperature Hydrodynamics Phenomena* (Academic Press, New York, 1966).

[56] B. Suryanarayana, R. J. Graybush, and J. R. Autera, *Chem. Ind. London* **52,** 2177 (1967).

[57] S. Bulusu, T. Axenrod, and G. W. A. Milne, *Org. Mass. Spectrom.* **3,** 13 (1970).

[58] M. Farber and R. D. Srivastava, in *16th JANNA Combus. Meeting*, Vol. 308 (CPIA pub., 1979), pp. 59.

[59] C. V. Morgan and R. A. Bayer, *Combust. Flame* **36,** 99 (1979).

[60] R. A. Fifer, in *Fundamentals of Solid Propellant Combustion, Progress in Astronautics and Aeronautics*, Vol. 90, edited by K. K. Kuo and M. Summerfield (AIAA Inc., New York, 1984), pp. 177.

[61] R. Behrens, *Int. J. Chem. Kinet.* **22,** 135 (1990).

[62] R. Behrens, *J. Phys. Chem.* **94,** 6706 (1990).

[63] R. Behrens and S. Bulusu, *J. Phys. Chem.* **95,** 5838 (1991).

64 J. C. Oxley, A. B. Kooh, R. Szekers, and W. Zhang, *J. Phys. Chem.* **98,** 7004 (1994).

65 T. B. Brill, P. E. Gongwer, and G. K. Williams, *J. Phys. Chem.* **98,** 12242 (1994).

66 T. B. Brill, *J. Prop. Power* **11,** 740 (1995).

67 C.-J. Tang, Y. J. Lee, G. Kudva, and T. A. Litzinger, *Combust. Flame* **117,** 170 (1999).

68 C.-J. Tang, Y. J. Lee, and T. A. Litzinger, *J. Prop. Power* **15,** 296 (1999).

69 D. D. Dlott, *Annual Reviews of Physical Chemistry* **50,** 251-278 (1999).

70 P. Politzer and S. Boyd, *Struct. Chem.* **13,** 105 (2002).

71 C. T. White, D. H. Robertson, M. L. Elert, and D. W. Brenner, in *Microscopic Simulations of Complex Hydrodynamic Phenomena*, edited by M. Mareschal and B. L. Holian (Plenum Press, New York, 1992), pp. 111.

72 D. W. Brenner, D. H. Robertson, M. L. Elert, and C. T. White, *Phys. Rev. Lett.* **70,** 2174 (1993).

73 C. F. Melius, in *Chemistry and Physics of Energetic Materials*, edited by D. N. Bulusu (Kluwer, Dordercht, 1990).

74 J. P. Lewis, K. R. Glaesemann, K. Van Opdorp, and G. A. Voth, *J. Phys. Chem. A* **104,** 11384 (2000).

75 D. Chakraborty, R. P. Muller, S. Dasgupta, and W. A. Goddard III, *J. Phys. Chem. A* **105,** 1302 (2001).

76 G. D. Smith and R. K. Bharadwaj, *J. Phys. Chem. B* **103,** 3570 (1999).

77 D. C. Sorescu, B. M. Rice, and D. L. Thompson, *J. Phys. Chem. B* **102,** 6692 (1998).

78 D. C. Sorescu, B. M. Rice, and D. L. Thompson, *J. Phys. Chem. B* **103,** 6783 (1999).

79 A. G. Landers and T. B. Brill, *J. Phys. Chem.* **84,** 3573 (1980).

80 L. E. Fried and W. M. Howard, *J. Chem. Phys.* **109,** 7338 (1998).

81 L. E. Fried and W. M. Howard, *Phys. Rev. B* **61,** 8734 (2000).

82 M. M. Kuklja, *J. Phys. Chem. B* **105,** 10159 (2001).

83 C. S. Yoo, W. J. Nellis, M. L. Sattler, and R. G. Musket, *Appl. Phys. Lett.* **61,** 273 (1992).

84 S. T. Weir, A. C. Mitchell, and W. J. Nellis, *Phys. Rev. Lett.* **76,** 1860 (1996).

85 W. J. Nellis, S. T. Weir, and A. C. Mitchell, *Science* **273,** 936 (1996).

86 A. Tokmakoff, M. D. Fayer, and D. D. Dlott, *J. Phys. Chem.* **97,** 1901 (1993).

87 M. D. Knudson and Y. M. Gupta, *Phys. Rev. Lett.* **81,** 2938 (1998).

88 K. Kadau, T. C. Germann, P. S. Lomdahl, and B. L. Holian, *Science* **296,** 1681 (2002).

89 T. C. Germann, B. L. Holian, P. S. Lomdahl, and R. Ravelo, *Phys. Rev. Lett.* **84,** 5351 (2000).

90 B. L. Holian and P. S. Lohmdahl, *Science* **280,** 2085 (1998).

91 V. V. Zhakhovskii, S. V. Zybin, K. Nishihara, and S. I. Anisimov, *Phys. Rev. Lett.* **83,** 1175 (1999).

92 E. J. Reed, L. E. Fried, and J. D. Joannopoulos, *Phys. Rev. Lett.* **90,** 2355031 (2003).

93 J. B. Maillet, M. Mareschal, L. Soulard, R. Ravelo, P. S. Lomdahl, T. C. Germann, and B. L. Holian, *Phys. Rev. E* **63,** 016121 (2001).

94 M. P. Allen and D. J. Tildesley, *Computer Simulation of Liquids* (Oxford University Press, New York, 1989).